Structural and Dynamic Determinants of Ligand Binding in the Ternary Complex of Chicken Liver Bile Acid Binding Protein with Two Bile Salts Revealed by NMR[†,‡]

Tommaso Eliseo,[§] Laura Ragona,[||] Maddalena Catalano,[||,⊥] Michael Assfalg,[⊥] Maurizio Paci,[§] Lucia Zetta,[||] Henriette Molinari,*[,⊥] and Daniel O. Cicero*[,§]

NMR Laboratory, Department of Chemical Science and Technology, University of Rome "Tor Vergata", 00133 Roma, Italy, NMR Laboratory, ISMAC-CNR, Via Bassini 15, 20131 Milano, Italy, and Dipartimento Scientifico e Tecnologico, Strada Le Grazie 15, University of Verona, 37134 Verona, Italy

Received July 3, 2007; Revised Manuscript Received August 28, 2007

ABSTRACT: Bile acids are physiological detergents facilitating absorption, transport, and distribution of lipid-soluble vitamins and dietary fats;they also play a role as signaling molecules that activate nuclear receptors and regulate cholesterol metabolism. Bile acid circulation is mediated by bile acid binding proteins (BABPs), and a detailed structural study of the complex of BABPs with bile salts has become a key issue for the complete understanding of the role of these proteins and their involvement in cholesterol homeostasis. The solution structure here reported describes, at variance with previously determined singly ligated structures, a BABP in a ternary complex with two bile acid molecules, obtained by employing a variety of NMR experiments. Exchange processes between the two bound chenodeoxycholate molecules as well as the more superficial ligand and the free pool have been detected through ROESY and diffusion experiments. Significant backbone flexibility has been observed in regions located at the protein open end, facilitating bile salts exchange. A detailed description of the protonation states and tautomeric forms of histidines strongly supports the view that histidine protonation modulates backbone flexibility and regulates ligand binding. This structure opens the way to targeted site-directed mutagenesis and interaction studies to investigate both binding and nuclear localization mechanisms.

Small lipophilic compounds play important roles in regulating biological functions (*1*). This is the case for bile acids, the amphipathic end products of cholesterol metabolism, which not only have a well-established role in dietary lipid absorption and cholesterol homeostasis but also were recently recognized to act as signaling molecules (*2*). Indeed they activate, among others, nuclear hormone receptors such as farnesoid X receptor α, thus regulating their own enterohepatic circulation, but also triglyceride, cholesterol, and glucose homeostasis. Thus, bile acid-controlled signaling pathways are promising novel drug targets to treat common metabolic diseases, such as obesity, type II diabetes, hyperlipidemia, and atherosclerosis (*2*). In addition to nuclear hormone receptors, bile acids bind in cells to intracellular lipid binding proteins (iLBP),[1] a family of small proteins (ca. 15 kDa) that, in spite of their remarkably similar β-barrel structures, diverge in their primary structure and in the selectivity exhibited toward different lipophilic ligands. Specifically bile acid binding proteins (BABP), belonging to the iLBP family, regulate transcellular trafficking of bile acids in hepatocytes and enterocytes, even though their mode of action is poorly understood. BABPs may also have specific functions in regulating the transcriptional activities of nuclear receptors with which they share a common ligand (*3*, *4*). Reported studies on the subcellular localization of some iLBPs (CRABP-II, K-FABP, and A-FABP) revealed that these proteins are indeed cytosolic in the absence of ligands but they translocate to the nucleus upon treatment of cells with appropriate ligands, thus suggesting that the structural basis for ligand-induced nuclear localization signals resides in a conformational change capable of enabling nuclear targeting (*1*). Within this framework, a detailed solution structural study of the topology of BABPs complexed with bile salts has become a key issue for the complete understanding of the role of these proteins. However, such solution structural studies represent a challenging task due to the presence of multiple ligands. Indeed BABPs have been reported to bind bile salts with a 1:2 stoichiometry (*5*, *6*), and such a stoichiometry was confirmed for the protein object of this study, namely, chicken liver BABP (cl-BABP) in complex with chenodeoxycholic acid (CDA) (*7*). We report

[†] This research was supported by FIRB 2003 (Grant RBNE03B8KK) and MIUR 2004 from the Italian Ministry for Education, University and Research.

[‡] The structure of cl-BABP ternary complex reported in this paper was deposited in the Protein Data Bank under filename 2JN3.

* Corresponding authors: (H.M.) tel +39 045 8027901, fax +39 045 8027929, e-mail molinari@sci.univr.it; (D.O.C.) tel +39 06 7259 4835, fax +39 06 7259 4328, e-mail cicero@scienze.uniroma2.it.

[§] University of Rome "Tor Vergata".

[||] NMR Laboratory, ISMAC-CNR.

[⊥] University of Verona.

[1] Abbreviations: cl-BABP, chicken liver bile acid binding protein; CDA, chenodeoxycholic acid; COSY, correlation spectroscopy; FID, free induction decay; HMQC, heteronuclear multiple quantum coherence; HSQC, heteronuclear single quantum coherence; iLBP, intracellular lipid binding proteins; NOESY, nuclear Overhauser effect spectroscopy; Pf1, filamentous phage; RDC, residual dipolar coupling; rmsd, root-mean-square deviation; ROESY, rotating Overhauser effect spectroscopy; TOCSY, total correlation spectroscopy; TEC, Trosy-E.Cosy; TROSY, transverse relaxation optimized spectroscopy.

10.1021/bi7013085 CCC: $37.00
Published on Web 10/11/2007

here the solution structure of cl-BABP ternary complex solved employing five distinct types of one-bond and two-bond residual dipolar couplings (RDC) measured by use of filamentous phage (Pf1) as alignment medium. In addition, diffusion coefficient measured for each of the two ligands, as well as for the protein, allowed us to detect the dynamic nature of the complex in solution. The analysis of histidine side-chain chemical shift changes, as a function of pH, allowed the investigation of their protonation equilibrium, playing an important role in modulating protein flexibility and regulating bile acids interaction (*8*). A comparison with previously determined singly ligated structures is reported.

EXPERIMENTAL PROCEDURES

NMR Spectroscopy. NMR experiments were performed on Bruker Avance700, Avance500, and Avance400 spectrometers equipped with triple-resonance probes and incorporating shielded *z*-axis gradient coils. Sequence schemes employing pulsed field gradients were employed to achieve suppression of the solvent signal and spectral artifacts. Selective pulses to cover aliphatic or aromatic or carbonyl ^{13}C nuclei spectral zone were obtained by adiabatic pulse modulation. Quadrature detection in the indirectly detected dimensions was obtained by the hybrid States-TPPI (time-proportional phase increment) method or the sensitivity-enhanced Echo−Anti-Echo combination. Linear prediction was applied to extend the indirect ^{13}C-detected dimension. Direct and indirect dimensions were normally apodized by use of 90°-shifted squared sine-bell functions (for ^{13}C-− and ^{15}N-edited dimensions) or Lorentzian-to-Gaussian functions (for ^{1}H dimension), followed by zero filling and Fourier transform. The NMR data were processed on Silicon Graphics workstations with NMRPipe (*9*) and analyzed with NMRView (*10*) software.

NMR Sample Preparation. Uniformly $^{15}N/^{13}C$-labeled cl-BABP was expressed and purified as previously described (*8*). Commercial CDA (Sigma−Aldrich) was employed for the preparation of holo-cl-BABP with a ligand to protein ratio of 3:1, following a published procedure (*11*). Final samples for NMR experiments contained 1.1 mM cl-BABP, 3 mM CDA, 30 mM sodium phosphate, pH 7.0, and 5 mM DTT (1,4-dithio-DL-threitol, from Sigma−Aldrich) in 90% H_2O/10% D_2O or 100% D_2O. All NMR experiments were conducted at 298 K.

Chemical Shift Assignment. The following standard set of triple resonance spectra were in H_2O: HNCO, HNCA, HN(CO)CA, CBCANH, and CBCA(CO)NH. For the sample dissolved in D_2O the following experiments were performed: (H)CCH-COSY, (H)CCH-TOCSY, H(C)CH-COSY, and H(C)CH-TOCSY. A ^{1}H-coupled (F_1) version of the HACACO experiment (*12*) was acquired in water. Side-chain resonance assignment was achieved for almost all nuclei and deposited together with the previously published backbone chemical shifts (*12*) in the BioMagResBank database (Accession Number 15084).

NOESY Experiments. A ^{15}N-edited 3D NOESY with mixing time of 150 ms and two ^{13}C-edited 3D NOESY spectra (one optimized for aliphatic residues and one for aromatic residues) with mixing times of 120 ms were recorded in H_2O. In order to detect intermolecular NOEs between the labeled protein and the unlabeled ligand, two F_1-edited, F_3-filtered 3D HMQC-NOESY spectra (*13*) were recorded in D_2O with mixing time 80 ms, optimizing carrier frequency, spectral widths, and delays to edit or filter ^{13}C magnetization arising from aliphatic and aromatic residues, respectively. A double-filtered [F_1-C/N,F_2-C/N] NOESY experiment (*14*) with mixing time of 80 ms was performed to filter out NOEs originating from the $^{15}N/^{13}C$-labeled protein. Finally, a 2D ^{1}H ROESY experiment was performed without ^{13}C decoupling in F_2 (with 50 ms of spin-locking time). No filter was applied to this experiment, in order to obtain the maximum sensitivity, and so protons belonging to the protein (appearing as doublets due to the $^{1}H-^{13}C$ coupling) as well as unlabeled CDA molecules are present.

RDC Measurements. Five distinct sets of RDCs were measured, namely, $^{1}J_{HN-N}$, $^{1}J_{H\alpha-C\alpha}$, $^{1}J_{C\alpha-C'}$, $^{1}J_{N-C'}$, and $^{2}J_{HN-C}$. Anisotropic data were collected by dissolving the holoprotein directly in 14 mg/mL liquid crystalline Pf1 (Asla Lab) as alignment medium. It was necessary to add NaCl up to 150 mM in order to decrease the signal line width. $^{1}J_{H\alpha-C\alpha}$ couplings were obtained from the HACACO experiment (*12*); $^{1}J_{N-C'}$ and $^{2}J_{HN-C'}$ were measured from $^{1}H-^{15}N$ HSQC spectra with only Cα decoupling (*15*); and $^{1}J_{HN-N}$ were measured in the Trosy-E.Cosy (TEC) experiment, based on the transverse relaxation optimized spectroscopy (TROSY) effect (*16*). $^{1}J_{H\alpha-C\alpha}$ couplings were measured in a ^{1}H-coupled (F_1) version of the HACACO experiment (*12*), and $^{1}J_{N-C'}$ and $^{2}J_{HN-C'}$ were measured from $^{1}H-^{15}N$ HSQC spectra with only Cα decoupling (*15*). $^{1}J_{C\alpha-C'}$ RDCs were measured in a modified version of the J-modulated HN(J-COCA) experiment (*17*) whose pulse sequence is reported in Figure 1 of Supporting Information. In this case we have used a HN−C′ 2D correlation, instead of the more popular HN−N correlation. The reason is 2-fold: it allows us to use the long constant time on the C′ nucleus (56.8 ms) to obtain a better resolution than the one achievable with the ^{15}N constant time (28 ms), and also because C′ dispersion is even higher than that of ^{15}N, allowing more resonances to be solved (*17*, *18*).

Diffusion Experiments. The PFG-STE (pulsed field gradient stimulated echo) experiment employing bipolar gradients (*19*) was conducted with 4 ms of gradient pulse duration. Delays of 50 and 150 ms between the defocusing and refocusing gradient elements were employed for experiments conducted on free CDA at pH 7.0 and on $^{15}N/^{13}C$-labeled cl-BABP complexed to CDA, respectively. A modified version of the same experiment was also performed, by concatenating the 1D version of the F_1-edited, F_3-filtered 3D HMQC-NOESY (*13*) to the PFG-STE pulse sequence (Figure 2 of Supporting Information) and using a delay of 80 ms between the pulsed field gradients. The length of all delays and pulses was held constant while the gradient strength was varied from 5% to 95% of its maximum value (53.5 G/cm). One important feature of this sequence is the total cancellation of signals arising from the free CDA, which is ensured by the phase cycling of the 90° and 180° ^{13}C pulses, allowing only signals originating from ^{1}H attached to ^{13}C to be detected. Additionally, the phase cycling on the first ^{1}H pulse cancels out the contribution of axial peaks that would originate from signals of free CDA that relaxes during the mixing time. Indeed, differently from what is normally used in a 3D experiment, a complete phase cycle of 64 steps was implemented for the 1D version.

Free induction decays were processed by applying a sensitivity-enhancement exponential function. Signal intensity was fitted to the following equation (*19*):

$$I_G = I_0 \exp\left[-D\gamma_H{}^2\delta^2 G^2\left(\Delta - \frac{\delta}{3}\right)\right]$$

where I_0 is the intensity in absence of gradients, D is the diffusion coefficient, γ_H is the proton magnetogyric ratio, δ is the duration of the gradient pulse, and Δ is the delay between the defocusing and refocusing gradients.

Histidine pH Titration. To investigate the tautomeric and protonation state of cl-BABP histidine residues, two $^1H-^{15}N$ long-range HSQC spectra were acquired at pH 7.0 and 4.0, respectively. For this experiment, the delay during which $^1H-^{15}N$ antiphase is produced was set to 22 ms, to refocus single-bond correlations. A series of constant-time $^1H-^{13}C$ HSQC spectra, optimized for the aromatic spectral region, was recorded at distinct pH values (pH 7.0, 6.5, 6.0, 5.4, 5.0, and 4.0). The observed chemical shifts of $H^{\epsilon 1}$ were plotted as a function of pH and fitted to the following equation (*20*) in order to evaluate pK_a values:

$$\delta_{obs} = \delta_d + \frac{\delta_p - \delta_d}{1 + 10^{(pH - pK_a)}}$$

where δ_p and δ_d are the chemical shifts of the protonated and deprotonated forms, respectively.

Structure Calculation. Structure calculation of cl-BABP complexed to two CDA molecules was performed with Xplor-NIH (*21*) and the PARALLHDG force field. The topology of H98 was modified to represent the $N^{\epsilon 2}$-protonated tautomer (see text below). Topology, force field parameters, and coordinates for the CDA were downloaded from the Hetero-compound Information Centre of Uppsala (http://xray.bmc.uu.se/hicup). Because CDA hydrogen atoms are not included in the mentioned parameter and coordinate files, a larger van der Waals radius was attributed to heavy atoms of the ligand molecules. First, the cl-BABP structure was generated in a completely extended conformation. Second, the protein and the two CDA molecules were allowed to anneal during a high-temperature search phase (3000 steps of molecular dynamics at 2000 K, 0.002 ps each step) by coupling the system to an external bath. Third, temperature was lowered up to 100 K in 127 cycles of cooling phase with steps of 0.002 ps. Last, 4000 steps of Powell energy minimization were executed. The simulated annealing was driven by NMR-derived constraints during all the calculation, with force constants and weighting factors optimized to increase the score of low-energy structures. A set of 1446 intraprotein and 216 protein−CDA distance restraints were used, subdivided into three groups: strong (1.8−3.3 Å), medium (1.8−4.5 Å), and weak NOEs (1.8−6.0 Å). Five distinct sets of backbone RDC ($^1J_{HN-N}$, $^1J_{H\alpha-C\alpha'}$, $^1J_{C\alpha-C'}$, $^1J_{N-C'}$, and $^2J_{HN-C}$) were included. Backbone ϕ and ψ dihedral angles were constrained to values predicted by TALOS (*22*). Backbone angles for residues K43, S51, K79, H83, A85, F96, and V116 were loosely constrained to standard values for the β-strand ($\phi = -120° \pm 40°$, $\psi = 110° \pm 40°$) as judged by the inspection of secondary structure elements in the previous rounds of the structure determination process. Backbone hydrogen bonds were recognized by evaluating the spatial relationship of amide protons with potential acceptors in the initial structures produced without the use of hydrogen bonds constraints. Two distance restraints were defined for each hydrogen bond: 1.8−2.3 Å for the HN−O distance and 2.3−3.3 Å for the N−O distance. In addition, specific side-chain hydrogen bonds were clearly individuated in most structures generated in later stages of the structural determination and employed as additional restraints in the last cycle of refinement (namely, $O^{\epsilon 2}$ of E39 with N^{ζ} of K52, $O^{\epsilon 2}$ of E109 with N^{ϵ} of R55, N^{ζ} of K76 with O-26 of CDA-II, and O-3 of CDA with O-7 of CDA-II). A statistically derived database of Ramachandran plot dihedral angles was used to improve the structural convergence. The statistics of structural geometry and of experimental constraints employed in calculations is summarized in Table 1. A complete cross-validation of RDCs was conducted by carrying out a series of simulated annealing calculations, each one lacking 10% of RDCs randomly chosen from the whole data set. The missing RDCs were back-calculated, in order to predict how well each RDC could be predicted: an average R_{free} of 24% was obtained (*23*). The ensemble of the 20 lowest global energy structures displaying violations of experimental constraints not greater than a defined threshold (0.5 Å for distance restraints, 1.0 Hz for H−N RDCs) was selected to represent the solution structure of the complex and deposited in the Protein Data Bank together with the corresponding constraint files (PDB code 2JN3). The programs AQUA and PROCHECK (*24*) were used to analyze the structures.

RESULTS AND DISCUSSION

Protein Resonances Assignment and Experimental Structural Constraints. The ^1H, ^{13}C, and ^{15}N backbone assignment of cl-BABP in complex with two CDA molecules was previously reported (*8*). In this study we have obtained the almost complete assignment of side chains for the holoprotein. The same result could not be achieved for the apo form of the protein, for which several side chains in the region 70−110 could not be assigned (*8*).

Chemical shift index analysis shows that the holo form of cl-BABP displays clear elements of secondary structure, divided into 10 β-strands and two α-helices. The strands comprise residues 5−12 (strand A), 37−43 (B), 47−53 (C), 56−62 (D), 68−72 (E), 76−85 (F), 90−93 (G), 95−103 (H), 105−112 (I), and 116−123 (J). In addition, the α-helices are composed of residues 14−20 (α1) and 25−32 (α2). The presence of these secondary structure elements was corroborated by analyzing the difference between the random-coil and observed $^1J_{H\alpha-C\alpha}$ (*12*) (Figure 5 of Supporting Information). A particularly low value was observed for $^1J_{H\alpha-C\alpha}$ of A22 (130 Hz), located in the loop connecting the two α-helices. This low value is a strong indication of a conformation showing a positive ϕ angle, and this constraint was introduced into the structure calculation.

Experimental constraints used to determine the protein fold, summarized in Table 1, included dihedral angles and interproton distances obtained from NMR experiments on a double-labeled protein in the presence of unlabeled ligands, as well as a large set of residual dipolar couplings, measured by use of Pf1 phage as alignment medium. Five RDCs per residue were measured, namely, $^1J_{HN-N}$, $^1J_{H\alpha-C\alpha}$, $^1J_{C\alpha-C'}$,

Table 1: Experimental Restraints and Structural Statistics for the 20 Lowest-Energy Structures of the Ternary Complex Cl-BABP/CDA

no. of experimental restraints	2503
distance restraints from NOEs	1662
intramolecular	1446
intraresidue	38
sequential	529
medium-range	276
long-range	603
intermolecular	213
hydrogen-bond distance restraints[a]	152
dihedral angle restraints	230
residual dipolar coupling constants	
H−N	102
$H_\alpha-C_\alpha$	100
C_α−CO	86
H−CO	83
N−CO	88
avg no. of restraints per residue	20.0
XPLOR energies (kcal/mol)	
E_{total}	980.2 ± 41.2
E_{bond}	3.70 ± 0.05
E_{angle}	132.67 ± 0.08
$E_{improper}$	22.38 ± 0.07
E_{vdw}	20.79 ± 0.96
E_{cdih}	1.9 ± 1.2
E_{rama}	453.3 ± 5.3
E_{noe}	133.1 ± 24.1
E_{sani}	212.4 ± 16.8
rms deviations from experimental restraints	
avg distance restraints violation (Å)	0.060 ± 0.005
avg no. of distance violation >0.2 Å	11.1[b]
avg dihedral angle restraints violation (deg)	0.34 ± 0.10
avg H−N RDC constants violation (Hz)	0.52 ± 0.05
avg $H_\alpha-C_\alpha$ RDC constants violation (Hz)	0.40 ± 0.04[c]
avg C_α−CO RDC constants violation (Hz)	2.07 ± 0.08[c]
avg H−CO RDC constants violation (Hz)	3.79 ± 0.05[c]
avg N−CO RDC constants violation (Hz)	2.65 ± 0.06[c]
R_{free} (%)	24 ± 3
rms deviations from idealized covalent geometry	
bond (Å)	0.0070 ± 0.0001
angle (deg)	0.734 ± 0.029
improper (deg)	0.625 ± 0.024
Ramachandran analysis	
residues in favored regions (%)	92.9 ± 1.0
residues in additional allowed regions (%)	7.1 ± 0.9
residues in generously allowed regions (%)	0.0 ± 0.0
residues in disallowed regions (%)	0.0 ± 0.0
coordinates precision[d] (Å)	
backbone	0.32 ± 0.05
all heavy atoms	0.79 ± 0.07

[a] HN−O and N−O distances were constrained to 2.1 ± 0.5 Å and 3.0 ± 0.5 Å, respectively. [b] Per structure. [c] Normalized with respect to the H−N value. [d] Rmsd with respect to the nonminimized average structure.

$^1J_{N-C'}$, and $^2J_{HN-C}$, as described under Experimental Procedures.

Assignment of the Two Bound Chenodeoxycholate Molecules. The chemical shift dispersion of protons belonging to CDA is very poor, but the presence of three methyl groups (C18, C19, and C21) (see Figure 3 of Supporting Information for atom numbering), which appear as high-intensity signals at relatively high fields (with reported chemical shifts of 0.67, 0.92, and 0.93 ppm) (*25*), constitutes a good entry point for the assignment of the bound molecules (Figure 1A). Filtered experiments can be used to eliminate ^{1}H signals belonging to the protein, which is ^{15}N- and ^{13}C-labeled, giving the possibility of observing the unlabeled ligands. Figure 1B shows the transformed first FID of the [F_1-C/N, F_2-C/N] NOESY experiment (*14*), which contains only signals of ^{1}H

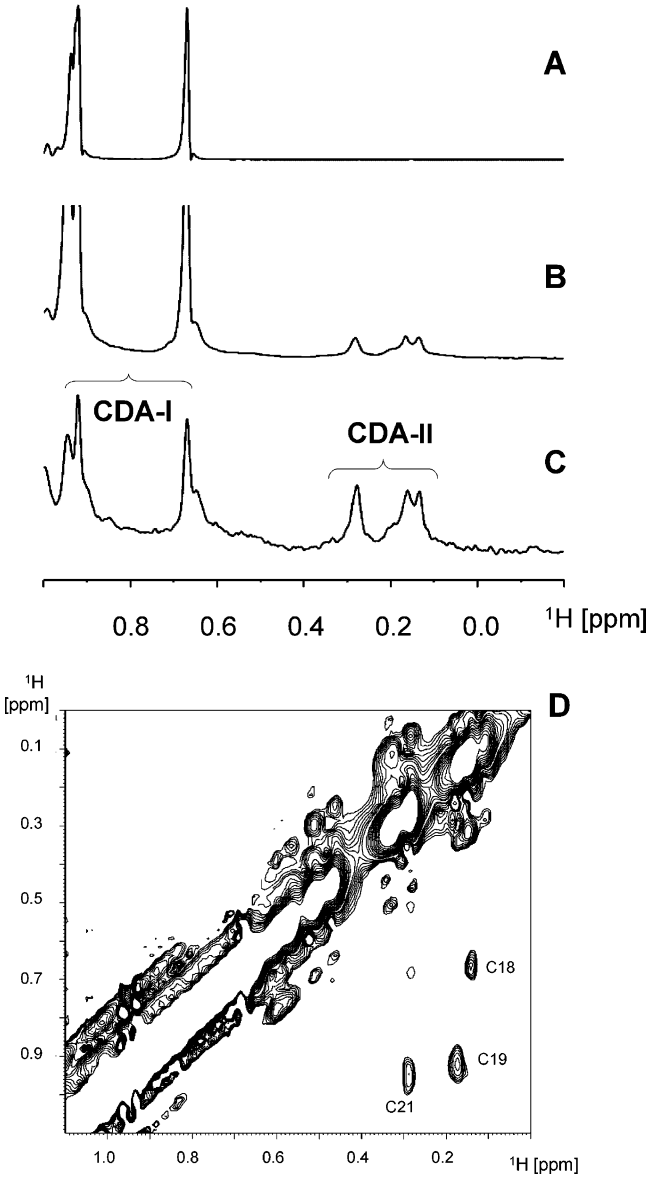

FIGURE 1: Analysis of methyl resonances of free and bound CDAs. (A) ^{1}H spectrum of free CDA. (B) Same region observed in the transformed first fid of the [F_1-C/N, F_2-C/N] NOESY, where resonances of ^{13}C-attached protons belonging to the protein are filtered. (C) Same region observed in the transformed first fid of the F_1-edited, F_3-filtered 3D HMQC-NOESY experiment. Only resonances of protons bound to ^{12}C and exhibiting NOE with protein protons are selected. (D) Selected region of the 2D-ROESY spectrum (mixing time 50 ms) showing exchange peaks between the three methyl groups of CDA-I and CDA-II.

bound to ^{12}C or ^{14}N. A comparison with spectrum of Figure 1A reveals three new broader signals at high fields, at 0.14, 0.17, and 0.28 ppm. In addition, three intense signals at the same chemical shift of free CDA were observed. As an excess of CDA was used to prepare the complex (1:3 cl-BABP/CDA), signals at 0.67, 0.92, and 0.95 ppm were tentatively assigned to free CDA. However, a total of six different methyl signals, in addition to those of free CDA, are expected if two molecules of CDA are bound to cl-BABP. An F_1-edited, F_3-filtered 3D HMQC-NOESY experiment (*13*) allowed us to specifically detect signals of bound CDA and eliminate those of the free form. Indeed, in this experiment, only ^{1}H signals of CDA experiencing NOE with the protein are detected. The Fourier-transformed first

FID is shown in Figure 1C. As can be clearly observed, the six methyl groups already present in Figure 1B are all experiencing NOE with the labeled cl-BABP. However, it is evident that the three methyl groups coinciding with free CDA show a smaller line width, strongly suggesting that there is a fast exchange between one of the bound molecules and free CDA. Independently of these observations, the strong similarity of chemical shifts between free CDA (Figure 1A) and the three downfield methyl groups (Figure 1B) allowed the assignment of C18, C19, and C21 of one of the two CDA molecules (here called CDA-I). A 2D ROESY experiment was performed to verify whether the two sets of signals showed any kind of exchange between them that would help in the assignment of the second bound form. Figure 1D shows a selected region of the ROESY experiment, indicating the presence of exchange peaks (with the same sign as the diagonal) between the two sets of methyl resonances. In this way we could assign the following resonances of the second bound molecule (CDA-II): 0.14 (C18), 0.17 (C19), and 0.28 (C21) ppm. The presence of exchange peaks can be explained either by a direct exchange between the two bound molecules or by an exchange between CDA-II and free CDA (see below). Structural models generated by use of intermolecular NOEs involving the already assigned methyl groups of CDA were used to interpret the whole set of protein−ligand NOEs and to complete the assignment of ligand resonances (see below).

Detecting Exchange of Bound CDA through Diffusion Measurements. One possible way of detecting exchange between bound and free states of CDA is through the measurement of the self-diffusion coefficient (*D*) (*26*). It is expected that a CDA molecule in exchange with the free form will show a *D* that is a linear combination of those of the free CDA and the protein. In order to measure the diffusion coefficient for the two CDA molecules, a stimulated echo with bipolar gradients has been added at the end of the 1D version of the F_1-edited, F_3-filtered 3D HMQC-NOESY experiment, which ensures that the self-diffusion coefficient to be measured corresponds only to molecules that are bound to the protein. A plot of signal intensity as a function of gradient strength for the two CDA molecules is shown in Figure 2. The experiment was repeated without the intermolecular selection for a sample containing only CDA in a concentration close to that expected for the excess of CDA in the sample of the complex, and for the complex sample but following methyl signals belonging to the protein. The calculated *D* values for free CDA and the holo form of the protein are 3.97×10^{-6} and 1.04×10^{-6} cm^2 s^{-1}, respectively. The values calculated for CDA-I and CDA-II are 1.85×10^{-6} and 1.10×10^{-6} cm^2 s^{-1}, respectively. From these values, it is possible to conclude that CDA-I is exchanging between the free and bound form, because the observed *D* is intermediate between those of free CDA and the protein. We can consider that the presence of the complex at a concentration of 1 mM will increase the viscosity of the solution. In this case, the expected *D* for the free CDA in the protein solution would be closer to that observed for CDA-I. The observed exchange of CDA-I is consistent with the presence of an exchange peak between the resonances of CDA-I and the free form in ^{15}N HSQC spectra of the unlabeled cl-BABP complexed with ^{15}N-glycochenodeoxycholic acid (*7*). On the other hand, the CDA-II *D* value, calculated from its signals, is almost coincident with that of the entire complex, thus indicating that the exchange with the free form is negligible. This result suggests that the exchange peaks detected in the ROESY spectrum are mostly due to an exchange process between the two bound molecules.

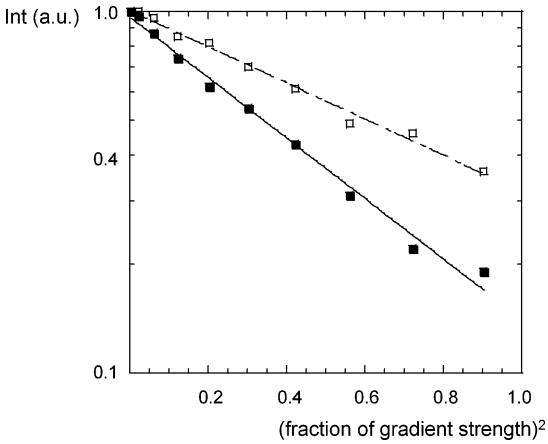

FIGURE 2: Analysis of diffusion experiments: self-diffusion coefficient (*D*) measurement following (■) the C18 signal of CDA-I and (□) the C21 signal of CDA-II. Dependence of the signal intensity (in logarithmic scale) is shown as a function of the square of the fraction of the gradient used. The calculated *D* values from these curves are 1.85×10^{-6} and 1.10×10^{-6} cm^2 s^{-1} for CDA-I and CDA-II, respectively.

Structure Calculation of the Ternary Complex between cl-BABP and Two Molecules of CDA. In the 3D F_1-edited, F_3-filtered HMQC-NOESY experiment (Figure 3A), displaying the intermolecular interactions, each of the already-described six methyl signals shows a number of NOEs with cl-BABP protons. These data were introduced as additional distance constraints for structure calculation. Subsequent rounds of refinement were used to identify further constraints from the 3D HMQC-NOESY spectrum, leading to the unambiguous assignment of ^{1}H in positions 1−8, 11, 12, 15−17, 20, 22, and 23 for CDA-I and positions 1−3, 7, 11, 15, and 16 of CDA-II.

A total of 115 NOE contacts between CDA-I and cl-BABP and 98 between CDA-II and cl-BABP were used to produce the final structures, together with 1446 intramolecular NOEs, 230 dihedral angle restraints, and 152 hydrogen-bond restraints. Evidence of fast motions for the α1−α2 region was derived from the HACACO experiments (see below); however, the S dependence of RDC to motional averaging anticipates only marginal deviations from the rigid structure situation (*27*).

Superposition of the 20 lowest energy structures is shown in Figure 3B, and Table 1 contains the statistical analysis of these structures. A remarkable convergence can be observed for both the protein and the two CDA molecules. Indeed, the overall rmsd for backbone and heavy atoms is 0.3 and 0.8 Å, respectively. These figures are at the lower limit of the range of values generally obtained for NMR structure calculations but are in line with other rmsd reported in the case of inclusion of a large set of RDC constraints (*28*, *29*). The WHATIF coarse and fine packing *Z*-scores are −0.87 and −1.36, respectively. Values larger than −2 are considered to represent good structures (*30*). These *Z*-scores, however, are not reflecting fairly the quality of the struc-

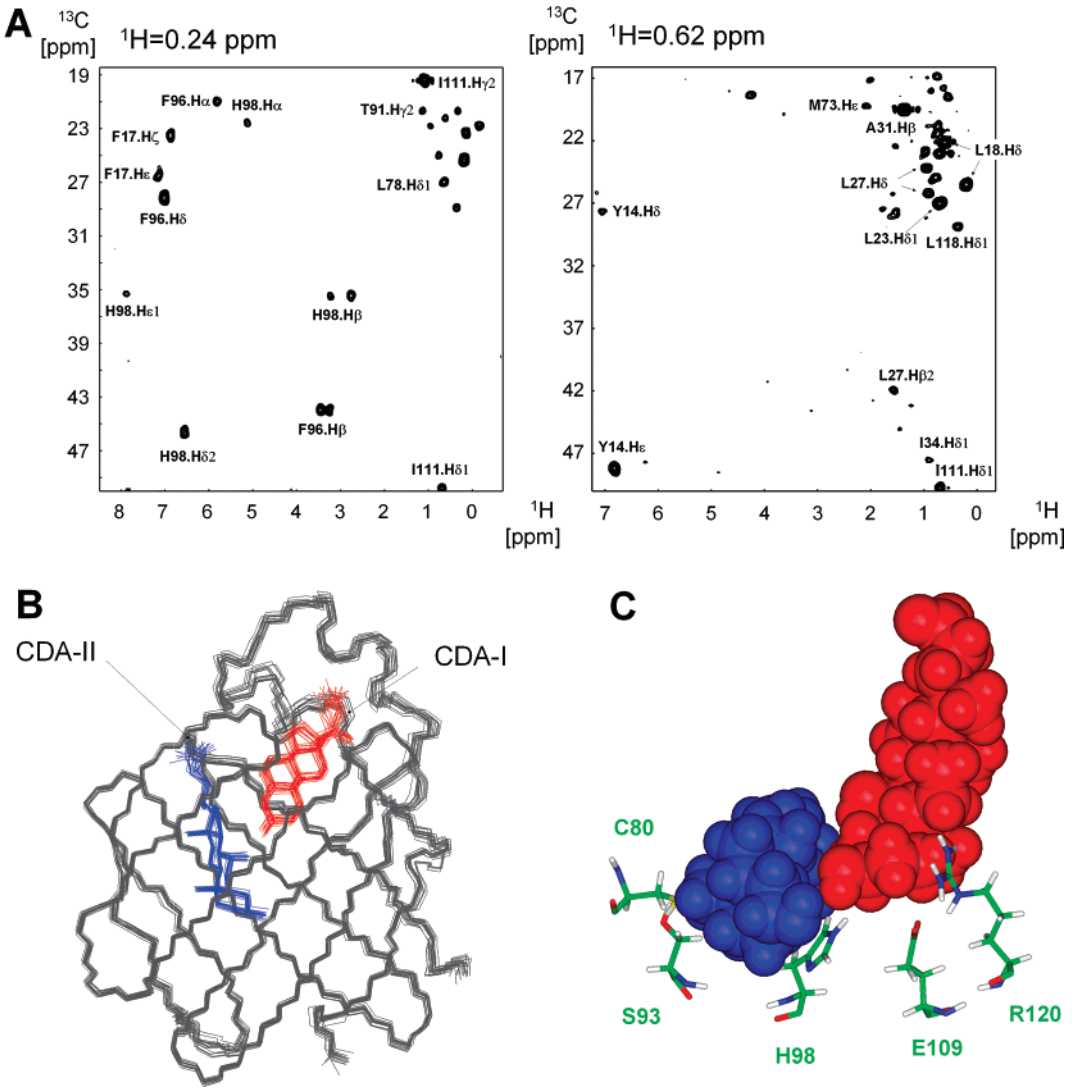

FIGURE 3: NMR and structural data of holo-cl-BABP. (A) F_1-F_2 slices of the F_1-edited, F_3-filtered 3D HMQC-NOESY experiment were used to determine intermolecular NOEs. Left and right panels correspond to the chemical shifts of C21 of CDA-II and C18 of CDA-I, respectively. Some of the assigned NOEs are indicated. A frequency folding was used in the F_2 dimension (^{13}C). (B) Superposition of the 20 lowest energy structures of the ternary complex between CDA and cl-BABP. The dotted line represents the intermolecular hydrogen bond between OH-3 of CDA-I and OH-7 of CDA-II used during structure calculations. (C) Polar spine and bound CDA molecules, represented with their van der Waals surface.

ture, because a large number of residues are in direct contact with the ligands, and no proper information can be obtained in the database regarding the likelihood of their conformations.

It is worth noting that no distance between the two CDA molecules could be used as constraint during the calculations. The only constraint in this respect is the presence of a hydrogen bond between OH-3 of CDA-I and OH-7 of CDA-II (see Figure 3B) that was detected in previous runs of refinement. Notably, intermolecular NOEs were measured for both M73-H$^{\epsilon}$ and the side chain of R55 with CDA-I C18, which were not employed during structure calculations because they were incompatible with the major set of interproton distances used, pointing to the existence of more than one conformation for CDA-I. ^{15}N HSQC spectra of the unlabeled cl-BABP complexed with ^{15}N glycochenodeoxycholic acid showed a double form for the resonance assigned to CDA-I, indicating the presence of two slightly different populations of the ligand at the superficial site, thus confirming the multiconformational state of CDA-I (*7*). Another clue to the dynamical nature of the complex was given by the presence of weak intermolecular NOEs between L18, L21, and L118 with methyl groups of CDA-II. In the structures, these three leucines are part of the hydrophobic cavity that binds CDA-I and are far away from CDA-II. The presence of these NOEs is in agreement with the proposed exchange between the two bound CDA molecules.

Analysis of the interactions between the ligands and the protein shows that both bile salt carboxylates are interacting with positively charged residues of the protein, namely, R55 (CDA-I) and K76 (CDA-II). The observed mobility of CDA-I matches the flexibility of the protein region comprising R55, which clearly shows the presence of fast motions. Figure 3C shows the close proximity of the two CDA molecules to the region defined as the polar spine, which through a hydrogen-bond network participates in the opening/closure mechanism of the protein (*8*). Several intermolecular NOEs were observed for C80 with CDA-II and for H98 with the two bound CDA molecules, thus supporting the role played by the spine residues in ligand binding.

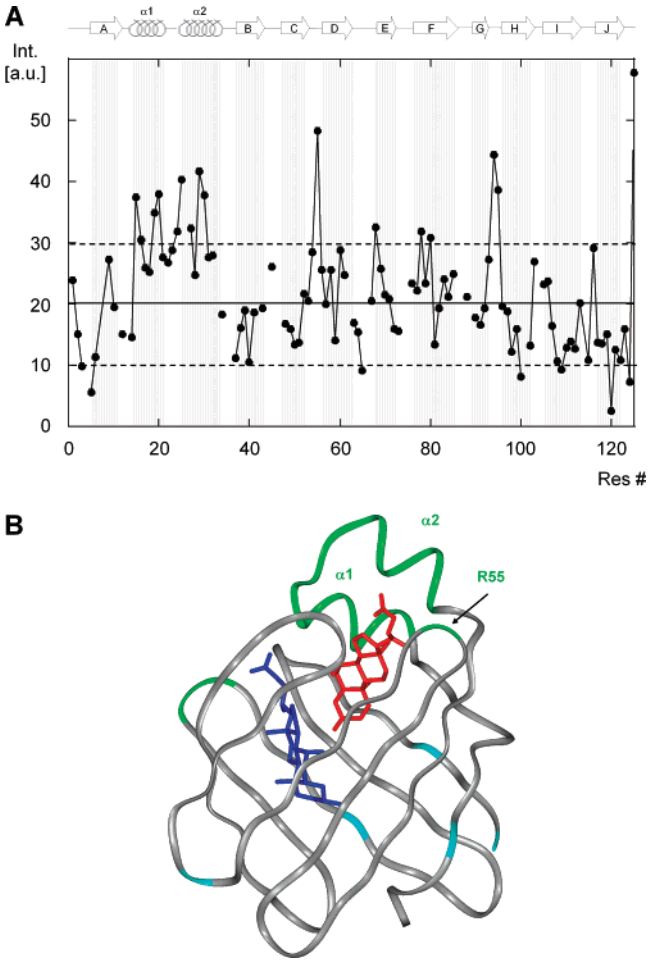

FIGURE 4: Dynamic behavior of holo-cl-BABP. (A) Observed intensity in the HACACO experiment as a function of residue number. Secondary structure elements of the protein are indicated. The horizontal solid line represents the average intensity, and the two broken lines are the average value ± 1 standard deviation. Residues showing values higher or lower than 1 standard deviation from the average are considered to experience motions in the pico- to nanosecond range or the micro- to millisecond range, respectively. (B) Mapping of dynamics on the holo structure: average structure for the ternary complex CDA-cl-BABP. CDA-I and CDA-II molecules are indicated in red and blue, respectively. Regions of the protein showing pico- to nanosecond or micro- to millisecond scale motions are indicated in green and cyan, respectively.

Dynamic Behavior of Holo-cl-BABP Analyzed through HACACO Intensity Measurements. The HACACO experiment was employed to monitor the backbone dynamics of the holo form of cl-BABP. As the chemical shift evolution of the Cα and C′ nuclei is performed in constant time, the main determinants of the cross-peak intensity are the Cα and C′ T_2 relaxation times (*12*, *31*). Inspection of the relative intensities in the 3D HACACO allows detection, in a simple way, of regions of the protein backbone experiencing motions. Indeed, cross-peak intensities larger or smaller by 1 standard deviation with respect to the average will highlight the presence of fast (pico- to nanosecond) or slow (micro- to millisecond) motions, respectively. In this line, the inspection of Figure 4Asuggests the presence of slow motions for residues 5, 100, 120, and 124. As a caveat, it should be noted that HACACO intensity measurements can provide only qualitative information, as variations in T_2 due to diffusional anisotropy are not taken into account. For this reason the obtained data were compared with the previously reported ^{15}N relaxation data on the holoprotein (*8*), and very good agreement is observed. On the other end, the region comprising residues 15−31, including the two α-helices and the loop connecting them, shows relatively high peak intensities, indicating the presence of fast motions. Residues 55 and 94−95, belonging to the CD and GH loops, respectively, as well as the C-terminal residue show mobility on the fast time scale (Figure 4). These results are significant as they reinforce previous data derived from Lipari−Szabo analysis (*8*).

The overall analysis of the dynamic behavior of cl-BABP reveals that the slow motion contributions observed for residues located in DE and EF loops and in FGHIJ strands of the apoprotein (*8*), are essentially quenched upon complexation. Thus ligand binding is expected to stabilize one conformation. Fast motions are not quenched in the holo conformation and remain confined to the helix−loop−helix region, which could act regulating the ligand entry into the cavity.

Histidine 98 Protonation State in Holo-cl-BABP. It was already suggested that the dynamical behavior of the apo form of cl-BABP depends on the protonation state of H98 (*8*). Indeed, ^{15}N relaxation measurements around a pH close to the pK_a of H98 (5.1) showed significant increase in micro- to millisecond motions for residues close to the histidine (*8*) upon decreasing the pH, suggesting that cl-BABP with protonated H98 is more flexible. These data, accompanied by NMR titration studies and molecular dynamics simulations performed at two different pH values, 7.0 and 5.6, with the histidines in the deprotonated and protonated forms, respectively, suggested that H98 protonation equilibrium could also be involved in the modulation of a functionally important motion, the opening/closure at the protein's open end.

For these reasons, we have focused our attention on the titration behavior of the two histidines, H83 and H98, in holo-cl-BABP. Figure 5Ashows the ^{1}H−^{15}N long-range HSQC spectra obtained at pH 7.0 (black spectrum) and pH 4.0 (red spectrum). Analysis of chemical shifts as well as connectivity patterns, based on reported histidine data analysis (*32*, *33*), indicates that at pH 7.0 H83 shows a mixture of different forms, including the deprotonated tautomer $N^{\delta 1}$ and the most abundant $N^{\epsilon 2}$ tautomer, together with a small population of the protonated form. Indeed, analysis of the chemical shifts observed for $H^{\epsilon 1}$ and $H^{\delta 2}$ as a function of pH allowed estimation of the population of the protonated form at each pH. H98, on the contrary, shows almost exclusively the $N^{\epsilon 2}$ deprotonated tautomer, characterized by the typical Γ pattern of the cross-peaks, with the expected chemical shifts for $N^{\delta 1}$ (252.5 ppm) and $N^{\epsilon 2}$ (161.7 ppm), and for the corresponding H^2 (7.84 ppm) and H^4 (6.56 ppm) protons (*34*) (Figure 5). The large difference in intensities also indicates that H83 possesses considerable mobility, whereas H98 is more conformationally constrained. Furthermore, at pH 4.0 H83 shows a predominance of the protonated form, while H98 does not show any significant change when compared to the situation at pH 7.0. The pH-dependent protonation of the two histidines was followed by recording constant-time ^{1}H−^{13}C HSQC spectra optimized for the aromatic region. Figure 5B shows the superposition of a series of spectra obtained at different pH values, ranging from 7.0 to 4.0. It

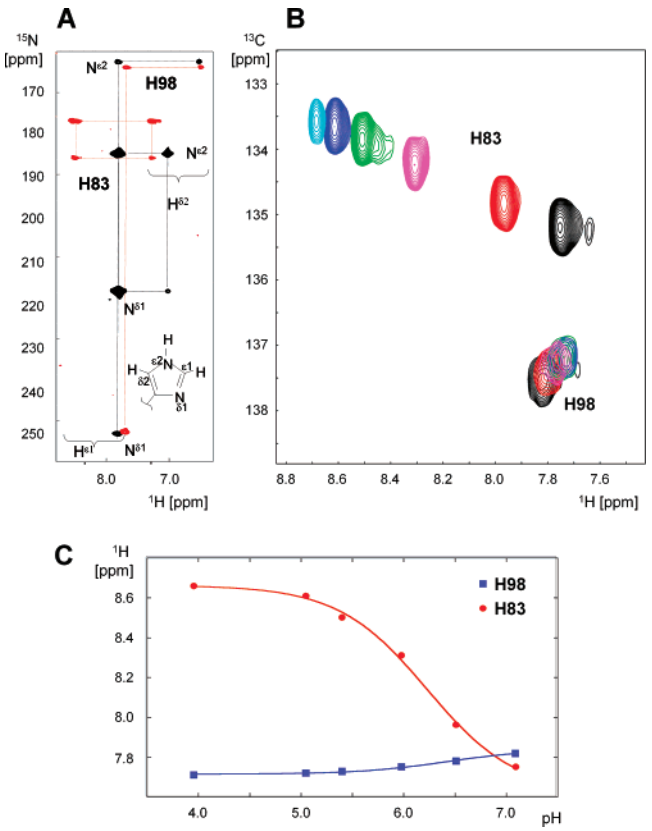

FIGURE 5: Analysis of the protonation states of histidine residues. (A) $^{1}H-^{15}N$ long-range HSQC spectra at pH 7.0 (black) and 4.0 (red). (B) Selected region of the $^{1}H-^{13}C$ constant-time HSQC experiment at pH 7.0 (black), 6.5 (red), 6.0 (magenta), 5.4 (green), 5.0 (blue), and 4.0 (cyan). (C) Titration curves for the $H^{\epsilon 1}$ resonance. Both histidine residues titrate with the same apparent pK_a of around 6.2. Titration of H98 is probably due to a long-range effect of H83 protonation.

can be noted that H83 $H^{\epsilon 1}$ shows a significant downfield shift with decreasing pH, whereas the same signal of H98 moves only marginally in the opposite direction. This behavior confirms that H83 is being titrated but H98 remains deprotonated in this range of pH. A plot of the observed chemical shift of $H^{\epsilon 1}$ as a function of pH for both histidines is shown in Figure 5C. Fitting of the observed titration data (*20*) allowed us to extract the pK_a value for H83, which was 6.23 ± 0.06, almost identical to that observed for the apo form (*8*). This value, in conjunction with the high mobility detected in the long-range $^{1}H-^{15}N$ HSQC, is compatible with the fact that this histidine is solvent-exposed. The corresponding proton of H98 moves only slightly upfield, and the apparent pK_a that can be fitted to this curve is very close to that of H83 (6.4 ± 0.1). Most likely, the observed shift is a long-range effect of H83 protonation, which is relatively close in the structure of cl-BABP. Taken all together, our data show that the pK_a of H98 is less than 4, because its protonation state does not change in the pH range 7.0−4.0. The observed drop of more than 1 unit in the pK_a value of H98 with respect to the apo form implies that complex formation strongly stabilizes the conformation showing H98 in the deprotonated state. Two main reasons can be the basis for such behavior: the formation of a strong hydrogen bond in which the nonprotonated nitrogen acts as an acceptor, or the position of the histidine in a buried region that renders the protonation more difficult. The relatively high chemical shift observed for the nonprotonated $N^{\delta 1}$ (253 ppm) seems to favor the second alternative (*35*). Indeed, this nitrogen does not point to any group that can act as a hydrogen donor. On the other hand, it is clearly located in a very hydrophobic pocket, surrounded by the two CDA molecules and with $N^{\delta 1}$ pointing directly to the plane of the GH β-strand. It is expected that the presence of the two ligands, in addition to hindering the solvent accessibility of the histidine, will strongly decrease the dielectric constant in the vicinity of H98, thereby destabilizing the positively charged protonated histidine in the absence of a nearby group acting as countercharge.

In general the very low H98 pK_a, measured for holoprotein, accompanied by the observation of reduced backbone motions in the holo state, strongly supports the hypothesis that the protonation of H98 induces protein flexibility.

Structural Comparisons. Interestingly, conformational changes occurring upon complexation are located at the protein open end and involve the helical (residues 15−28) and EF regions (residues 72−80) showing average global backbone rmsd higher than 2 Å (see Figure 4 of Supporting Information) It is interesting to note that the EF loop is the region mostly affected by binding also in human and pig ileal BABPs implying that this large movement enables the opening/closure of the protein cavity.

The comparison of the obtained structure (cl-BABP complexed with two CDAs) with the one obtained by X-ray for cL-BABP complexed with two cholate (CA) molecules (*36*) shows a very good agreement, with an average rmsd of 0.87 Å relative to the backbone superposition and an rmsd of 0.66 Å and 0.40 Å relative to the superficial and internal ligands, after proteins superposition, as obtained with the PROFIT program (*40*). CDA and CA differ in the hydroxylation at position 12 (see Figure 3 of Supporting Information for atom numbering). This hydroxyl group is indeed important because it allows the internal molecule of CA to establish H-bonds with the side chain of H98 and/or with the hydroxyl group in position 3 of CA-I. Nonetheless, only slight changes in the protein structure are observed upon binding of the two different molecules. Among these, M73 shows a different conformation in the two complexes. The absence of the OH-12 group in the CDA molecule allows the ϵ-CH_3 group of M73 to get closer to CDA-I, whereas in the CA complex the methionine side chain moves away to accommodate the hydroxyl group. The long and flexible side chain of this amino acid is particularly well suited to adapt itself to different ligands, as the well-documented mechanism of target recognition by calmodulin has already established (*37*).

A more significant difference between the two structures is the conformation of H98. A comparison between the regions around this residue is shown in Figure 6. It can be noticed that H98, although occupying the same spatial region in the two structures, shows a reversed orientation in the CDA complex with respect to that described for the CA complex (*36*). The difference between the conformation that H98 adopts in the two complexes could be the result of the presence of the OH-12 group in the cholate molecule. Indeed, a hydrogen bond between OH-12 of the internal CA molecule and the nonprotonated $N^{\delta 1}$ could stabilize this conformation (Figure 6), but such interaction is absent in the CDA complex. Still, we cannot exclude that the orientation of H98 is the same in the two complexes, because while NMR can

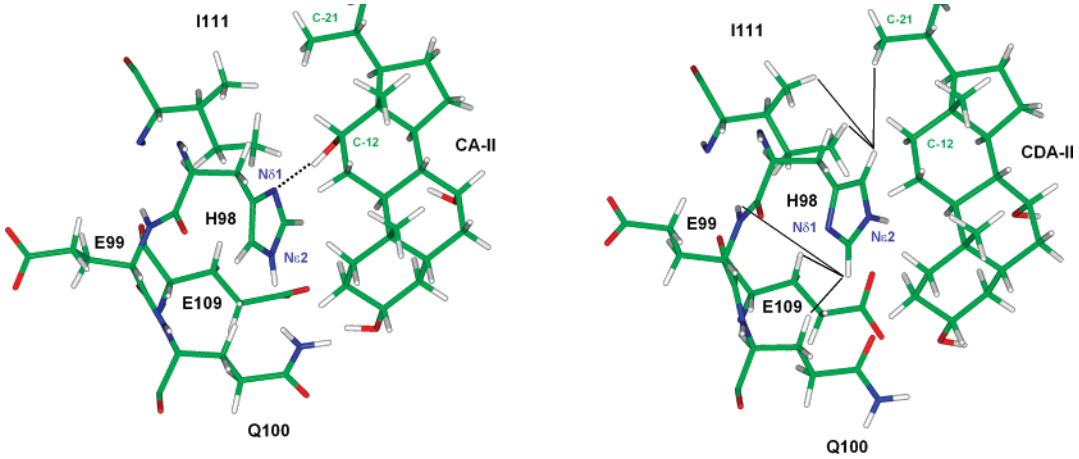

FIGURE 6: Comparison between X-ray and NMR structures. H98 shows a reversed orientation in the two complexes. (Left) CA complex, where the dotted line represents a hydrogen bond between OH-12 of CA-II and Nδ1. (Right) CDA complex, where solid lines represent the observed NOEs between H98 and different side chains of CDA-II.

accurately define the actual orientation of the ring, given that the resonances of $H^{\delta 2}$ and $H^{\epsilon 1}$ are very different, the electron densities of N and C are very similar and may not be distinguishable. In addition, a number of unambiguous NOEs support the H98 orientation here described for the CDA complex, in particular those regarding H98-$H^{\delta 2}$ with the C21 methyl of CDA-II and with I111, and strong NOEs between H98-$H^{\epsilon 1}$ with E99 HN, Q100, and E109 side chains (Figure 6).

The structure here reported is the first obtained by NMR for a ternary complex of a bile acid binding protein with two bile acids. Indeed the previously reported NMR structures of holo pig and human ileal BABPs (PDB codes 1EIO and 1O1V, respectively) referred to singly ligated forms (*38*, *39*). These structures were obtained at temperatures where the observation of one of the two ligand molecules was hampered by NMR exchange broadening, thus missing the description of the functional form of holo-BABPs in complex with two molecules of bile salts (*6*). The superposition of cl-BABP holo structure with the singly ligated forms of human and pig ileal BABPs shows that the single glycocholate molecule, bound to the pig ileal BABP, corresponds to CDA-II molecule of cl-BABP (Figure 7A), with a different arrangement of the sterol moiety. On the other hand, the single taurocholate molecule is bound to the human ileal protein in such a way that the first cyclohexane ring almost coincides with that of CDA-II, while the taurine moiety occupies part of binding site of CDA-I (Figure 7B). The results obtained for both pig and human ileal BABPs can be explained by the presence of chemical exchange between the more superficial ligand and the free pool and between the two bound bile acids, as here demonstrated for CDAs bound to cl-BABP.

In conclusion, by use of specifically tailored NMR experiments, a high-resolution solution structure of a challenging ternary system was obtained together with a description of the dynamic nature of this complex for which exchange between the two binding sites as well as between one binding site and the free pool is observed. This dynamic behavior was shown to match flexibility in two protein regions facilitating this exchange. The unique capability of NMR spectroscopy to detect protonation states and tautomeric forms of histidine residues allowed us to describe in detail the protonation equilibrium of one histidine playing an important role in modulating molecular flexibility and regulating ligand binding (*8*). The acquired structural details about the network of polar buried residues involved in this mechanism further complement the functional description of the system. The solution structure of this ternary complex of a bile acid binding protein with two bile acids now opens the way to targeted site-directed mutagenesis and interaction studies to investigate both binding and nuclear localization mechanisms.

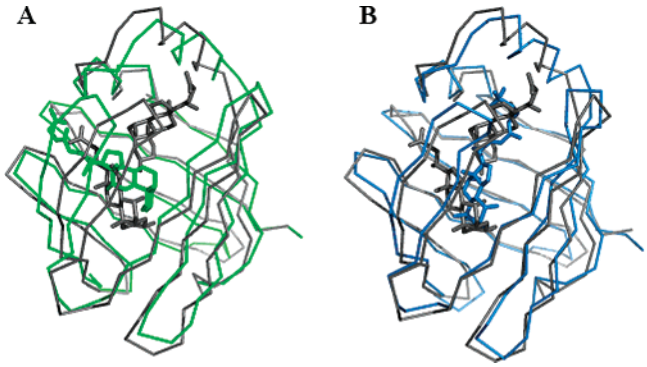

FIGURE 7: Comparison of the NMR structure of cl-BABP in complex with two molecules of CDA (gray, PDB code 2JN3) with the singly ligated structures obtained for (A) pig ileal-BABP in complex with glycocholate (green, PDB code 1EIO) and (B) human ileal BABP in complex with taurocholate (light blue, PDB code 1O1V). The displayed structures are the first (lowest energy) structures of each family. The average rmsd of the ligand molecules within each family was calculated after all-atom fitting with the Profit software, obtaining values of 0.60 Å (CDA-II, 10 structures, this work), 0.66 Å (CDA-I, 10 structures, this work), 1.52 Å (1EIO, 5 structures), and 0.926 Å (1O1V, 10 structures).

ACKNOWLEDGMENT

We appreciate the support of the Large Scale Facility SONNMR of Utrecht University. CIRMMP (Consorzio Interuniversitario di Risonanze Magnetiche di Metalloproteine Paramagnetiche), is gratefully acknowledged.

SUPPORTING INFORMATION AVAILABLE

Description of pulse sequences for the measurement of (i) $^1J_{C\alpha-C'}$ by HN−C′ 2D correlation and (ii) self-diffusion coefficient of ^1H signals bound to ^{12}C or ^{14}N and experiencing NOE with the protein; numbering for the bile acid; plot of

global backbone rmsd between apo and holo structures; and plot of the differences between observed $^1J_{H\alpha-C\alpha}$ and random coil values for all residues of the proteins. This material is available free of charge via the Internet at http://pubs.acs.org

REFERENCES

1. Sessler, R. J., and Noy, N. (2005) A ligand-activated nuclear localization signal in cellular retinoic acid binding protein-II, *Mol. Cell 18*, 343−353.
2. Houten, S. M., Watanabe, M., and Auwerx, J. (2006) Endocrine functions of bile acids, *EMBO J. 25*, 1419−1425.
3. Chawla, A., Saez, E., and Evans, R. M. (2000) "Don't know much bile-ology", *Cell 103*, 1−4.
4. Chiang, J. Y. (2002) Bile acid regulation of gene expression: roles of nuclear hormone receptors, *Endocr. Rev. 23*, 443−463.
5. Kurz, M., Brachvogel, V., Matter, H., Stengelin, S., Thuring, H., and Kramer, W. (2003) Insights into the bile acid transportation system: the human ileal lipid-binding protein-cholyltaurine complex and its comparison with homologous structures, *Proteins: Struct., Funct., Genet. 50*, 312−328.
6. Tochtrop, G. P., Richter, K., Tang, C., Toner, J. J., Covey, D. F., and Cistola, D. P. (2002) Energetics by NMR: site-specific binding in a positively cooperative system, *Proc. Natl. Acad. Sci. U.S.A. 99*, 1847−1852.
7. Tomaselli, S., Ragona, L., Zetta, L., Assfalg, M., Ferranti, P., Longhi, R., Bonvin, A. M. J. J., and Molinari, H. (2007) NMR-based modelling and binding studies of a ternary complex between chicken liver bile acid binding protein and bile acids, *Proteins: Struct., Funct., Bioinf. 69*(*1*), 177−191.
8. Ragona, L., Catalano, M., Luppi, M., Cicero, D., Eliseo, T., Foote, J., Fogolari, F., Zetta, L., and Molinari, H. (2006) NMR dynamic studies suggest that allosteric activation regulates ligand binding in chicken liver bile acid-binding protein, *J. Biol. Chem. 281*, 9697−9709.
9. Delaglio, F., Grzesiek, S., Vuister, G. W., Zhu, G., Pfeifer, J., and Bax, A. (1995) NMRPipe: a multidimensional spectral processing system based on UNIX pipes, *J. Biomol. NMR 6*, 277−293.
10. Johnson, B. A. (2004) Using NMRView to visualize and analyze the NMR spectra of macromolecules, *Methods Mol. Biol. 278*, 313−352.
11. Tochtrop, G. P., DeKoster, G. T., Covey, D. F., and Cistola, D. P. (2004) A single hydroxyl group governs ligand site selectivity in human ileal bile acid binding protein, *J. Am. Chem. Soc. 126*, 11024−11029.
12. Cicero, D. O., Contessa, G. M., Paci, M., and Bazzo, R. (2006) HACACO revisited: residual dipolar coupling measurements and resonance assignments in proteins, *J. Magn. Reson. 180*, 222−228.
13. Lee, W., Revington, M. J., Arrowsmith, C., and Kay, L. E. (1994) A pulsed field gradient isotope-filtered 3D ^{13}C HMQC-NOESY experiment for extracting intermolecular NOE contacts in molecular complexes, *FEBS Lett. 350*, 87−90.
14. Ikura, M., and Bax, A. (1992) Isotope-filtered 2D NMR of a protein−peptide complex: study of a skeletal muscle myosin light chain kinase fragment bound to calmodulin, *J. Am. Chem. Soc. 114*, 2433−2440.
15. Wang, Y.-X., Marquardt, J. L., Wingfield, P., Stahl, S. J., Lee-Huang, S., Torchia, D., and Bax, A. (1998) Simultaneous Measurement of ^{1}H−^{15}N, ^{1}H−^{13}C′, and ^{15}N−^{13}C′ Dipolar Couplings in a Perdeuterated 30 kDa Protein Dissolved in a Dilute Liquid Crystalline Phase, *J. Am. Chem. Soc. 120*, 7385−7386.
16. Eliseo, T., Gallo, M., Melis, R., Paci, M., Bazzo, R., and Cicero, D. O. (2006) Single scan TROSY and E:COSY suite of experiments for the measurements of residual dipolar couplings in proteins, *Spectroscopy 20*, 153−167.
17. McFeeters, R. L., Fowler, C. A., Gaponenko, V. V., and Byrd, R. A. (2005) Efficient and precise measurement of H^{α}—C^{α}, C^{α}—C′, C^{α}—C^{β} and H^N−N residual dipolar couplings from 2D H^N−N correlation spectra, *J. Biomol. NMR 31*, 35−47.
18. Caffrey, M., Kaufman, J., Stahl, S. J., Wingfield, P. T., Gronenborn, A. M., and Clore, G. M. (1998) 3D NMR experiments for measuring ^{15}N relaxation data of large proteins: application to the 44 kDa ectodomain of SIV gp41, *J. Magn. Reson. 135*, 368−372.
19. Altieri, A. S., Hinton, D. P., and Byrd, R. A. (1995) Association of Biomolecular Systems via Pulsed Field Gradient NMR Self-Diffusion Measurements, *J. Am. Chem. Soc. 117*, 7566−7567.
20. Hass, M. A., Thuesen, M. H., Christensen, H. E., and Led, J. J. (2004) Characterization of μs-ms dynamics of proteins using a combined analysis of ^{15}N NMR relaxation and chemical shift: conformational exchange in plastocyanin induced by histidine protonations, *J. Am. Chem. Soc. 126*, 753−765.
21. Schwieters, C. D., Kuszewski, J. J., Tjandra, N., and Clore, G. M. (2003) The Xplor-NIH NMR molecular structure determination package, *J. Magn. Reson. 160*, 65−73.
22. Cornilescu, G., Delaglio, F., and Bax, A. (1999) Protein backbone angle restraints from searching a database for chemical shift and sequence homology, *J. Biomol. NMR 13*, 289−302.
23. Lakomek, N. A., Carlomagno, T., Becker, S., Griesinger, C., and Meiler, J. (2006) A thorough dynamic interpretation of residual dipolar couplings in ubiquitin, *J. Biomol. NMR 34*, 101−115.
24. Laskowski, R. A., Rullmannn, J. A., MacArthur, M. W., Kaptein, R., and Thornton, J. M. (1996) AQUA and PROCHECK-NMR: programs for checking the quality of protein structures solved by NMR, *J. Biomol. NMR 8*, 477−486.
25. Waterhous, D. V., Barnes, S., and Muccio, D. D. (1985) Nuclear magnetic resonance spectroscopy of bile acids. Development of two-dimensional NMR methods for the elucidation of proton resonance assignments for five common hydroxylated bile acids, and their parent bile acid, 5 beta-cholanoic acid, *J. Lipid Res. 26*, 1068−1078.
26. Stockman, B. J., and Dalvit, C. (2002) NMR screening techniques in drug discovery and drug design, *Progress in Nucl. Magn. Reson. Spectrosc. 41*(*3*−*4*), 187−231.
27. Bryce, D. L., and Bax, A. (2004) Application of correlated residual dipolar couplings to the determination of the molecular alignment tensor magnitude of oriented proteins and nucleic acids, *J. Biomol. NMR 28*, 273−287.
28. Bewley, C. A., Gustafson, K. R., Boyd, M. R., Covell, D. G., Bax, A., Clore, G. M., and Gronenborn, A. M. (1998) Solution structure of cyanovirin-N, a potent HIV-inactivating protein, *Nat. Struct. Biol. 5*, 571−578.
29. Legler, P. M., Cai, M., Peterkofsky, A., and Clore, G. M. (2004) Three-dimensional solution structure of the cytoplasmic B domain of the mannitol transporter $II^{mannitol}$ of the *Escherichia coli* phosphotransferase system, *J. Biol. Chem. 279*, 39115−39121.
30. Vriend, G. (1990) WHAT IF: a molecular modeling and drug design program, *J. Mol. Graphics 8*, 52−56.
31. Cicero, D. O., Contessa, G. M., Pertinhez, T. A., Gallo, M., Katsuyama, A. M., Paci, M., Farah, C. S., and Spisni, A. (2007) Solution structure of ApaG from *Xanthomonas axonopodis* pv. citri reveals a fibronectin-3 fold, *Proteins: Struct., Funct., Bioinf. 67*(*2*), 490−500.
32. Sudmeier, J. L., Ash, E. L., Gunther, U. L., Luo, X., Bullock, P. A., and Bachovchin, W. W. (1996) HCN, a triple-resonance NMR technique for selective observation of histidine and tryptophan side chains in ^{13}C/^{15}N-labeled proteins, *J. Magn. Reson. B 113*, 236−247.
33. Van Dijk, A. A., Scheek, R. M., Dijkstra, K., Wolters, G. K., and Robillard, G. T. (1992) Characterization of the protonation and hydrogen bonding state of the histidine residues in IIAmtl, a domain of the phosphoenolpyruvate-dependent mannitol-specific transport protein, *Biochemistry 31*, 9063−9072.
34. Coggins, B. E., McClerren, A. L., Jiang, L., Li, X., Rudolph, J., Hindsgaul, O., Raetz, C. R., and Zhou, P. (2005) Refined solution structure of the LpxC-TU-514 complex and pK_a analysis of an active site histidine: insights into the mechanism and inhibitor design, *Biochemistry 44*, 1114−1126.
35. Bachovchin, W. W. (1986) ^{15}N NMR spectroscopy of hydrogen-bonding interactions in the active site of serine proteases: evidence for a moving histidine mechanism, *Biochemistry 25*, 7751−7759.
36. Nichesola, D., Perduca, M., Capaldi, S., Carrizo, M. E., Righetti, P. G., and Monaco, H. L. (2004) Crystal structure of chicken liver basic fatty acid-binding protein complexed with cholic acid, *Biochemistry 43*, 14072−14079.
37. Anbanandam, A., Bieber Urbauer, R. J., Bartlett, R. K., Smallwood, H. S., Squier, T. C., and Urbauer, J. L. (2005) Mediating molecular recognition by methionine oxidation: conformational switching by oxidation of methionine in the carboxyl-terminal domain of calmodulin, *Biochemistry 44*, 9486−9496.

38. Lucke, C., Zhang, F., Hamilton, J. A., Sacchettini, J. C., and Ruterjans, H. (2000) Solution structure of ileal lipid binding protein in complex with glycocholate, *Eur. J. Biochem. 267*, 2929−2938.
39. Kramer, W., Glombik, H., Petry, S., Heuer, H., Schafer, H., Wendler, W., Corsiero, D., Girbig, F., and Weyland, C. (2000) Identification of binding proteins for cholesterol absorption inhibitors as components of the intestinal cholesterol transporter, *FEBS Lett. 487*, 293−297.
40. Martin, A. C. R. ProFit, http://www.bioinf.org.uk/software/profit.

BI7013085